**Integrated Systems and Technologies**

# Kinetic Modeling and Constrained Reconstruction of Hyperpolarized [1-13C]-Pyruvate Offers Improved Metabolic Imaging of Tumors

James A. Bankson[1], Christopher M. Walker[1,2], Marc S. Ramirez[1], Wolfgang Stefan[1], David Fuentes[1], Matthew E. Merritt[3], Jaehyuk Lee[1], Vlad C. Sandulache[4], Yunyun Chen[5], Liem Phan[6], Ping-Chieh Chou[6], Arvind Rao[7], Sai-Ching J. Yeung[8], Mong-Hong Lee[6], Dawid Schellingerhout[9,10], Charles A. Conrad[11], Craig Malloy[3], A. Dean Sherry[3], Stephen Y. Lai[5,6], and John D. Hazle[1]

## Abstract

Hyperpolarized [1-13C]-pyruvate has shown tremendous promise as an agent for imaging tumor metabolism with unprecedented sensitivity and specificity. Imaging hyperpolarized substrates by magnetic resonance is unlike traditional MRI because signals are highly transient and their spatial distribution varies continuously over their observable lifetime. Therefore, new imaging approaches are needed to ensure optimal measurement under these circumstances. Constrained reconstruction algorithms can integrate prior information, including biophysical models of the substrate/target interaction, to reduce the amount of data that is required for image analysis and reconstruction. In this study, we show that metabolic MRI with hyperpolarized pyruvate is biased by tumor perfusion and present a new pharmacokinetic model for hyperpolarized substrates that accounts for these effects. The suitability of this model is confirmed by statistical comparison with alternates using data from 55 dynamic spectroscopic measurements in normal animals and murine models of anaplastic thyroid cancer, glioblastoma, and triple-negative breast cancer. The kinetic model was then integrated into a constrained reconstruction algorithm and feasibility was tested using significantly undersampled imaging data from tumor-bearing animals. Compared with naïve image reconstruction, this approach requires far fewer signal-depleting excitations and focuses analysis and reconstruction on new information that is uniquely available from hyperpolarized pyruvate and its metabolites, thus improving the reproducibility and accuracy of metabolic imaging measurements. *Cancer Res; 75(22); 1–10. ©2015 AACR.*

## Introduction

Visualization of hyperpolarized (HP) substrates by magnetic resonance (MR) enables interrogation of biologic systems with unprecedented spatial resolution and chemical specificity. Amplification of the excess spin population of an MR-visible label by up to four orders of magnitude through dissolution dynamic nuclear polarization (DNP) generates signal enhancement in a bolus injectable solution (1) that is preserved through chemical reactions, permitting measurement of HP agents and their metabolites on a time scale that was previously impossible. [1-13C]-pyruvate is the most widely studied HP substrate to date, due to its relatively long relaxation time, rapid distribution and uptake, and the central role that pyruvate plays in metabolism. Glucose, the most abundant source of fuel in normal tissue, is catabolized to pyruvate by intracellular enzymes. In normal tissue, most pyruvate is converted into acetyl-CoA by pyruvate dehydrogenase and subsequently oxidized for production of reducing equivalents and generation of ATP. Under anaerobic conditions, or if glycolysis is pathologically upregulated as in many cancers that display the "Warburg" effect (2, 3), excess pyruvate is rapidly exchanged with lactate via lactate dehydrogenase (LDH) and cofactor nicotinamide adenine dinucleotide (NADH). Pyruvate can also exchange with alanine via alanine aminotransferase in a non-redox–dependent fashion. Thus the chemical conversion of HP [1-13C]-pyruvate can provide powerful insight into the metabolic state of tumor tissue and provide an index of metabolic flux changes due to gene expression (4) or response to therapy (5, 6).

These measurements are technically challenging in part because they are highly transient. The HP signal is a fixed resource that is established by the polarizer, and cannot be renewed after injection. Signal is continuously lost via spin–lattice relaxation ($T_1 <$

[1]Department of Imaging Physics, The University of Texas MD Anderson Cancer Center, Houston, Texas. [2]The University of Texas Graduate School of Biomedical Sciences, Houston, Texas. [3]Advanced Imaging Research Center, The University of Texas Southwestern Medical Center, Houston, Texas. [4]Department of Otolaryngology, Baylor College of Medicine, Houston, Texas. [5]Department of Head and Neck Surgery, The University of Texas MD Anderson Cancer Center, Houston, Texas. [6]Department of Molecular and Cellular Oncology, The University of Texas MD Anderson Cancer Center, Houston, Texas. [7]Department of Bioinformatics and Computational Biology, The University of Texas MD Anderson Cancer Center, Houston, Texas. [8]Department of Emergency Medicine, The University of Texas MD Anderson Cancer Center, Houston, Texas. [9]Department of Diagnostic Radiology, The University of Texas MD Anderson Cancer Center, Houston, Texas. [10]Department of Cancer Systems Imaging, The University of Texas MD Anderson Cancer Center, Houston, Texas. [11]Department of Neuro-Oncology, The University of Texas MD Anderson Cancer Center, Houston, Texas.

60 s *in vivo*) and depleted by exchange and signal excitation. After injection, HP agents must distribute through tissue, overcome biologic transport barriers, and interact with target physiology. Acquisition strategies must be carefully designed to ensure that spatial and temporal information are sampled appropriately to yield robust, reproducible, and physiologically meaningful results. If an excessive portion of the spin pool is depleted too early then signal from downstream products will be compromised. If imaging data are sampled after the injected substrate has been depleted, then the opportunity for quantitative or ratiometric evaluation may be lost. If the sampling strategy is distributed over time, then assumptions of data consistency implicit in traditional image reconstruction by Fourier transform may be violated, risking the potential for confounding artifacts. "Single-shot" imaging methods can acquire images over a time interval where the distribution of HP agents remains relatively constant. However, these approaches require excitations that consume a larger fraction of the HP signal and may limit subsequent observations, and data acquisition at high bandwidth may compromise image quality. Alternative imaging strategies are critically needed to ensure that HP agents are optimally measured. We propose a model-based reconstruction algorithm that incorporates temporal information about HP substrate evolution, via pharmacokinetic modeling, and spatial information from ^{1}H MRI, to allow reconstruction of dynamic HP images from data that is, in the traditional sense, severely undersampled in time and space.

Such an approach requires a reasonable kinetic model for signal evolution. A first-order, two-site model has been previously used to quantify the apparent rate of conversion of HP pyruvate into lactate in cells and *in vivo* (6–10). HP pyruvate is converted into lactate at an apparent rate that depends on the intracellular equilibrium concentrations of pyruvate, lactate, LDH, and NADH (11, 12). Several groups have integrated terms to account for inflow of HP agents (13–15), including direct measurement (16) of the vascular input function (VIF). With no separation between physical pools, these models assume that all observed HP agents are in direct chemical contact with enzymes that catalyze exchange, leading to overestimation of chemically active HP pyruvate and underestimation of the apparent rate of conversion. More complex multicompartment models have been shown to accurately represent signal evolution in cells (17).

In this study, we examine kinetic models for HP [1-^{13}C]-pyruvate and their use in a constrained reconstruction algorithm for improved reconstruction of dynamic multidimensional data. Kinetic models are compared in murine models of anaplastic thyroid cancer (ATC), triple-negative breast cancer, and glioblastoma. We select the kinetic model that gives maximal fidelity to experimental data with minimal complexity and computational burden. Prior information from traditional ^{1}H MRI is used to reduce the number of unknown model parameters that must be determined from dynamic HP ^{13}C data. We show that model-based constrained reconstruction allows dynamic images to be visualized at arbitrary spatiotemporal resolution from a limited set of radial projections that are distributed over the observable lifetime of the HP signal. The ability to reconstruct the dynamic image space with fewer signal excitations adds a new degree of freedom for optimization of HP imaging protocols, thus improving the quality of data and diagnostic potential of this modality.

## Materials and Methods

All experiments involving animals were reviewed and approved by our Institutional Animal Care and Use Committee to ensure adherence to guidelines put forth by the PHS Policy on Humane Care and Use of Laboratory Animals and the National Research Council Guide for the Care and Use of Laboratory Animals.

### Animals bearing anaplastic thyroid cancer

Male athymic nude mice were purchased from the NCI. U-HTH83 luciferase expressing cells were obtained from the laboratory of Dr. Jeffrey N. Myers (Department of Head and Neck Surgery, The University of Texas MD Anderson Cancer Center, Houston, TX) and authenticated using short tandem repeat analysis within six months of experiments. A total of $2.5 \times 10^5$ cells were orthotopically injected into the right thyroid lobe as previously described (18). Tumors were allowed to establish for 7 to 9 days before imaging experiments.

### Animals bearing triple-negative breast cancer with inducible expression of stratifin

MDA-MB-231 triple-negative breast cancer cells were obtained from ATCC within 6 months of use. A total of $1 \times 10^6$ cells carrying a Tet-On inducible stratifin expression were injected into the mammary fat pad of female nude mice. Four weeks after implantation, animals were given normal drinking water or water containing 200 μg/mL doxycycline and the effect of stratifin expression on conversion of HP pyruvate to lactate (19) was tested 2 weeks later.

### Animals bearing glioblastoma

U87 human-derived glioblastoma cells were obtained from ATCC within 6 months of experiments. A total of $1 \times 10^6$ cells were injected into the right caudoputamen of nude mice by means of stereotactic injection through an implanted plastic intracranial bolt. Tumors were allowed to grow for approximately 30 days until suitable in size for imaging.

### Dynamic nuclear polarization

Hyperpolarized [1-^{13}C]-pyruvate was prepared using a HyperSense dissolution DNP system (Oxford Instruments). Of note, 26 mg aliquots of [1-^{13}C]-pyruvic acid (Cambridge Isotopes) containing 1.5 mmol/L Gadoteridol (Bracco Diagnostics) and 15 mmol/L OX63 (GE Healthcare) were cooled to 1.45K in a 3.35T magnetic field, and irradiated at approximately 94.13 GHz for 45 minutes or until solid-state polarization levels reached a plateau. The frozen substrate was then dissolved in 4 mL of 180°C distilled water containing 80 mmol/L NaOH, 50 mmol/L NaCl, 0.1 g/L EDTA, and 40 mmol/L Trizma pre-set crystals (pH 7.6), resulting in a 37°C isotonic solution containing 80 mmol/L HP [1-^{13}C]-pyruvate. Once dissolution was complete, 200 μL of the solution was drawn and administered to animals via tail-vein catheter.

### Dynamic ^{13}C magnetic resonance spectroscopy

All spectroscopic measurements were carried out using a 7T Biospec small animal MR system, with BGA-12 gradients and a ^{1}H/^{13}C dual-tuned volume coil with 72 mm inner diameter (ID; Bruker Biospin MRI). Animals were anesthetized using isoflurane and placed on an imaging sled with integrated channels for anesthesia and warm circulating water to maintain body temperature. A fast spin–echo (FSE) sequence (TR = 2500 ms,

TE$_{Eff}$ = 16.7 ms, 8 echoes) was used to visualize tumor location. Dynamic $^{13}$C spectroscopy was acquired using a slice-selective pulse-acquire sequence (TR = 2,000 ms, 10°–15° excitation, 8 mm slice thickness, 90 repetitions, spectral width = 4960 Hz, number of spectral points = 2,048) with excitation through the $^{13}$C channel of the volume coil and signal reception using a 15-mm ID surface coil placed over the tumor. The dynamic acquisition was initiated by the HyperSense system during dissolution, approximately 18 seconds before injection.

### Dynamic $^{13}$C magnetic resonance spectroscopic imaging

Two dynamic $^{13}$C spectroscopic imaging protocols were implemented to explore the effects of variations in prior information that could be incorporated into the constrained reconstruction algorithm. The hardware was configured as described above for dynamic $^{13}$C spectroscopy experiments. In both cases, dynamic $^{13}$C imaging data were acquired using a radial multiband frequency encoding (radMBFE) sequence (20, 21) with golden angle increments (111.246°) between projections.

In one set of experiments, the radMBFE sequence (TR = 750 ms, 20° excitation, 8 mm slice thickness) was modified to incorporate interleaved acquisition of data for constrained estimation of the VIF. One slice was prescribed over the tumor and doubly refocused with adiabatic inversion pulses (TE = 135 ms; ref. 22), and another slice was prescribed through the heart and recalled by gradient echo (TE = 22.2 ms; ref. 23). The 35-mm field of view was encoded by 86.4 Hz/cm readout gradients, with 5.3 spectral bands over a total readout bandwidth of 1,602 Hz. Data acquisition was initiated after injection of HP pyruvate in order to avoid interference between inversion pulses and spins flowing into the volume coil.

The second set of measurements used a gradient-echo radMBFE sequence (TE = 16.1 ms, TR = 1,000 ms, 20° excitation, 8 mm slice thickness) that permitted acquisition of data starting before injection of HP pyruvate. A slightly smaller readout FOV of 30 mm allowed use of stronger readout gradients (100.7 Hz/cm) and the total bandwidth was extended (7.9 bands over 2,394 Hz) in order to accommodate a fiducial marker containing 8 mol/L $^{13}$C-enriched urea. Coregistered dynamic contrast-enhanced (DCE-) MRI scans were subsequently acquired to inform on parameters in the kinetic model for $^{13}$C substrate evolution.

Radially encoded $^1$H gradient-echo imaging data (TR = 200 ms, TE = 1.4 ms) with matching field of view and slice locations were acquired immediately after all dynamic $^{13}$C acquisitions to confirm animal positioning throughout the protocol and provide additional information about the span of image space occupied by tissue to the constrained reconstruction.

### Dynamic contrast-enhanced MRI

Two DCE-MRI protocols were also used in this work. Initial experiments testing the relationship between HP lactate signal and tumor perfusion were conducted with HP measurements on the 7T system followed by dynamic MRI on a nearby 4.7T Biospec with BG-6 gradients, a $^1$H volume coil with 35 mm ID, and sequences that were optimized for DCE-MRI as previously described (23). Dynamic data were acquired using a fast, spoiled gradient-echo (FSPGR) sequence (TE = 1.55 ms, TR = 40.7 ms, 30° excitation, 128×96 image matrix) with seven Cartesian-encoded slices dedicated to tumor imaging interleaved with one radially-encoded section for constrained estimation of the VIF with temporal resolution of 2×TR.

For proof-of-principle coregistered dynamic $^1$H imaging and $^{13}$C spectroscopic imaging data, some sacrifice in the quality of DCE-MRI data was permitted to allow both measurements to be collected at 7T within the same scanning session and without changing the hardware configuration. Dynamic data were acquired using the $^1$H channel of the dual-tuned $^1$H/$^{13}$C volume resonator with 72 mm ID. The duty cycle for the FSPGR sequence was reduced to avoid overheating the larger imaging gradients by increasing the repetition time (TE = 1.67 ms, TR = 75 ms, 35° excitation, 96×64 image matrix) and by acquiring data from only three slices that spanned the 8-mm extent of the excitation slice used for $^{13}$C imaging. In this data, the VIF was measured through manual identification of intravascular voxels near the tumor.

### Kinetic model

The conversion of HP pyruvate into lactate *in vivo* is often semiquantitatively summarized using normalized lactate (nLac), defined as the ratio of HP lactate to the sum of HP pyruvate and lactate signals. Given that the observable HP signal has a lifetime of only a few passes of circulation, we hypothesized that tumor perfusion would significantly affect nLac. To investigate this relationship, we acquired dynamic spectra of HP [1-$^{13}$C]-pyruvate and DCE-MRI in ATC tumors challenged with 2-deoxyglucose (2DG, 500 mg/kg given i.p. 2h prior to scans; $N = 4$) or sham therapy ($N = 3$). 2DG is a competitive inhibitor of glycolysis with no acute mechanistic link to changes in tumor vascular function. After acquisition of dynamic HP $^{13}$C spectra at 7T, animals were scanned at 4.7T for assessment of tumor perfusion. The results summarized in Fig. 1 show the anticipated reduction in chemical conversion following metabolic challenge with 2DG and a strong linear relationship between the normalized lactate signal and tumor permeability. These results indicate that nLac is not a strictly independent readout of aerobic glycolysis and that a more advanced model must account for the vascular compartment and extravasation of the HP substrate.

We therefore consider the three candidate pharmacokinetic models illustrated in Fig. 2 to help describe the evolution of signal and separate the parameter reflecting aerobic glycolysis, $k_{pl}$, from confounding nuisance parameters. These models are composed of two chemical pools and one to three physical compartments. The two-site precursor-product model in Fig. 2A is similar to nLac in that it assumes all observed substrate has the ability to interact with intracellular enzymes that enable exchange. In Fig. 2B, intravascular space is separated from an extravascular space that is assumed to be homogenized by very rapid diffusion and membrane transport. The most accurate biophysical model is shown in Fig. 2C, where intravascular, extravascular/extracellular, and intracellular compartments are separate and transfer of the $^{13}$C label between chemical pools can only occur in the latter. This model also involves the largest number of unknown parameters, which increases the computational burden and expected variance in fitted parameters.

For brevity, only the differential equations for the model with two physical and two chemical pools (Fig. 2B), are shown:

$$\frac{\partial Pyr_{ev}(t)}{\partial t} = -\left(\frac{k_{ve}}{v_e} + k_{pl} + R_{Pyr} + \frac{1-\cos\theta}{TR}\right)Pyr_{ev}(t) + k_{lp}Lac_{ev}(t) + \frac{k_{ve}}{v_e}Pyr_{iv}(t) \quad (1)$$

$$\frac{\partial Lac_{ev}(t)}{\partial t} = k_{pl}Pyr_{ev}(t) - \left(\frac{k_{ve}}{v_e} + k_{lp} + R_{Lac} + \frac{1-\cos\theta}{TR}\right)Lac_{ev}(t) + \frac{k_{ve}}{v_e}Lac_{iv}(t) \quad (2)$$
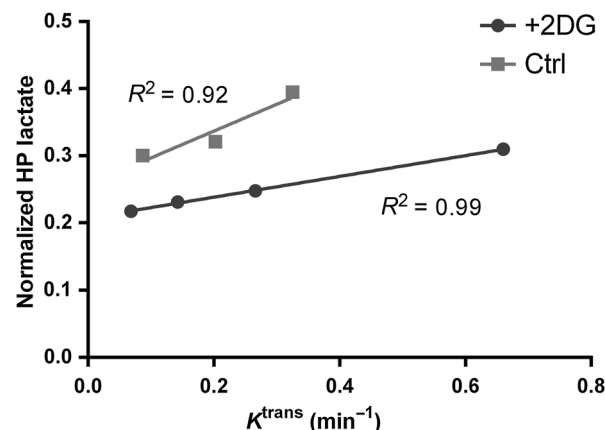
Bankson et al.



**Figure 1.**
Relationship between the nLac signal and tissue perfusion ($K^{trans}$) assessed by DCE-MRI in a murine model of ATC. Although differences in nLac were not quite statistically significant ($P = 0.08$; $t$ test) and no differences in $K^{trans}$ were observed between groups, strong correlation between perfusion and nLac is evident.

$Pyr_{iv}(t)$ and $Pyr_{ev}(t)$ indicate the time-dependent intravascular and extravascular HP pyruvate concentrations, respectively, with corresponding notation for HP lactate. Extravasation and clearance of agents occur at rate $k_{ve}$, modified by the extracellular volume fraction $v_e$ to ensure conservation of spins across physical boundaries. The apparent rate constant for chemical conversion of HP pyruvate to lactate is given by $k_{pl}$, and the reverse reaction rate by $k_{lp}$. $R_{Pyr}$ and $R_{Lac}$ reflect losses due to $T_1$ relaxation and biologic endpoints that are outside of our focus. The solution to equations (1 and 2) is found by the variation of parameters method:

$$\begin{bmatrix} Pyr_{ev}(t) \\ Lac_{ev}(t) \end{bmatrix} = e^{At} \begin{bmatrix} Pyr_{ev}(t=0) \\ Lac_{ev}(t=0) \end{bmatrix} + \frac{k_{ve}}{v_e} \int_0^t e^{A(t-\tau)} \begin{bmatrix} Pyr_{iv}(\tau) \\ Lac_{iv}(\tau) \end{bmatrix} d\tau, \quad (3)$$

where

$$\mathbf{A} = \begin{bmatrix} -\left(\frac{k_{ve}}{v_e} + k_{pl} + R_{Pyr} + \frac{1-\cos\theta}{TR}\right) & k_{lp} \\ k_{pl} & -\left(\frac{k_{ve}}{v_e} + k_{lp} + R_{Lac} + \frac{1-\cos\theta}{TR}\right) \end{bmatrix} \quad (4)$$

In general, unless specifically sought (24, 25), the physical compartment from which these signals originate cannot be determined. The total observed signal is the weighted sum from individual compartments:

$$\begin{bmatrix} Pyr(t) \\ Lac(t) \end{bmatrix} = \begin{bmatrix} Pyr_{ev}(t) & Pyr_{iv}(t) \\ Lac_{ev}(t) & Lac_{iv}(t) \end{bmatrix} \begin{bmatrix} v_e \\ v_b \end{bmatrix} \quad (5)$$

The vascular blood volume fraction is given by $v_b$. In the special case with $Pyr_{ev}(t=0) = Lac_{ev}(t=0) = 0$, $k_{lp} = 0$, and $Lac_{iv}(t) = 0$, equations (3–5) simplify considerably:

$$Pyr(t) = k_{ve} \int_0^t e^{\alpha_{Pyr}(t-\tau)} Pyr_{iv}(\tau) d\tau + v_b Pyr_{iv}(t), \quad (6)$$

$$Lac(t) = \frac{k_{ve} \cdot k_{pl}}{\alpha_{Lac} - \alpha_{Pyr}} \int_0^t \left\{ e^{\alpha_{Lac}(t-\tau)} - e^{\alpha_{Pyr}(t-\tau)} \right\} Pyr_{iv}(\tau) d\tau, \quad (7)$$

where

$$\alpha_{Pyr} = -\left(\frac{k_{ve}}{v_e} + k_{pl} + R_{Pyr} + \frac{1-\cos\theta}{TR}\right),$$
$$\alpha_{Lac} = -\left(\frac{k_{ve}}{v_e} + R_{Lac} + \frac{1-\cos\theta}{TR}\right) \quad (8)$$

Equation (6) can be recognized as very similar to the well-established extended Tofts model for kinetic analysis of DCE-MRI
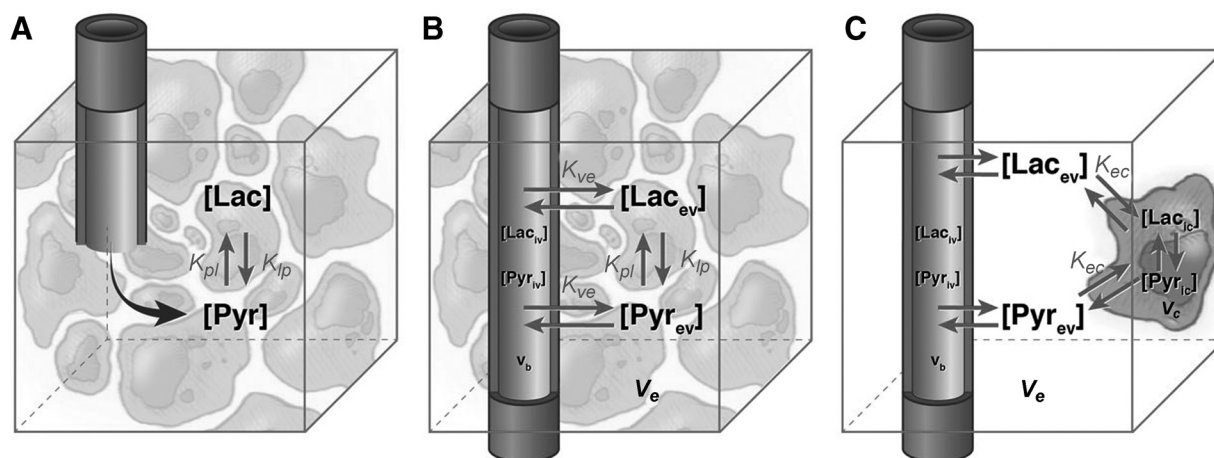


**Figure 2.**
Candidate kinetic models to describe dynamic signal evolution of HP pyruvate and lactate *in vivo*. All models include two chemical pools and one spatial compartment (A), two spatial compartments (intravascular and extravascular) with exchange limited to extravascular region (B), or three spatial compartments (intravascular, extravascular/extracellular, and intracellular) with exchange restricted to the intracellular region (C).

data (26, 27). Pyruvate extravasates from vasculature with a rate constant $k_{ve}$ as $T_1$-reducing contrast agents extravasate with $K^{trans}$ in DCE-MRI measurements, while clearance terms ($\alpha$) here include effects that are unique to the HP spin pools. Given a VIF that is directly measured or assumed in form, perfusion and apparent chemical conversion rates can be jointly estimated from dynamic data using these equations.

The model summarized in Fig. 2B and derived above is clearly an approximation, implicitly assuming a homogeneous extravascular environment. Model C (Fig. 2C) more accurately describes the system, with six pools composed of HP pyruvate and lactate in distinct vascular, extravascular/extracellular, and intracellular compartments. It is described by:

$$
\begin{bmatrix} Pyr_{ev}(t) \\ Lac_{ev}(t) \\ Pyr_{ic}(t) \\ Lac_{ic}(t) \end{bmatrix} = e^{At} \begin{bmatrix} Pyr_{ev}(t=0) \\ Lac_{ev}(t=0) \\ Pyr_{ic}(t=0) \\ Lac_{ic}(t=0) \end{bmatrix} + \int_0^t e^{A(t-\tau)} \begin{bmatrix} Pyr_{iv}(\tau) \\ Lac_{iv}(\tau) \\ 0 \\ 0 \end{bmatrix} d\tau, \quad (9)
$$

with

$$
\mathbf{A} = \begin{bmatrix} -\left(\dfrac{k_{ve}}{v_{ee}} + \dfrac{k_{ec}}{v_{ee}} + R_{Pyr} + \dfrac{1-\cos\theta}{TR}\right) & 0 & \dfrac{k_{ec}}{v_{ee}} & 0 \\[2mm] 0 & -\left(\dfrac{k_{ve}}{v_{ee}} + \dfrac{k_{ec}}{v_{ee}} + R_{Lac} + \dfrac{1-\cos\theta}{TR}\right) & 0 & \dfrac{k_{ec}}{v_{ee}} \\[2mm] \dfrac{k_{ec}}{v_c} & 0 & -\left(\dfrac{k_{ec}}{v_c} + k_{pl} + R_{Pyr} + \dfrac{1-\cos\theta}{TR}\right) & k_{lp} \\[2mm] 0 & \dfrac{k_{ec}}{v_c} & k_{pl} & -\left(\dfrac{k_{ec}}{v_c} + k_{lp} + R_{Lac} + \dfrac{1-\cos\theta}{TR}\right) \end{bmatrix} \quad (10)
$$

Here, HP pyruvate and lactate are assumed to exchange between extravascular/extracellular and intracellular compartments, with volume fractions $v_{ee}$ and $v_c$ respectively, at rate $k_{ec}$.

### Model comparison and selection

The models illustrated in Fig. 2 were implemented in Matlab (The Mathworks). Dynamic $^{13}$C spectra were fit to these models by minimizing the residual mean-square difference between measured and modeled curves. Conversion from lactate to pyruvate was assumed negligible ($k_{lp} = 0$) and, in the model composed of three physical pools, transport of HP lactate across the cell membrane was also assumed negligible. For models corresponding to Fig. 2B and C, intravascular pyruvate was assumed in the form of a gamma-variate curve (28) with variable amplitude, shape, and delay from the start of data acquisition. To minimize the impact of local minima, the parameter space was logarithmically sampled over the range of likely parameter values and the set that yielded the lowest residual difference was used as the seed for further optimization. A bound constrained quasi-Newton optimization was used, with gradients of the residual computed by finite differences.

Akaike's information criterion (AIC; ref. 29) was used to compare and select among candidate models. This framework rewards a model that fits observed data well and penalizes the inclusion of additional free parameters. AIC can be calculated as:

$$
AIC = n\ln\left\{ \frac{1}{n}\sum_t \left[ S'(\mathbf{p},t) - S(t) \right]^2 \right\} + 2K\left( \frac{n}{n-K-1} \right) \quad (11)
$$

Here, estimates ($S'(\mathbf{p},t)$) of $n$ samples of the signal $S(t)$, are provided by a given kinetic model with a vector of parameters, $\mathbf{p}$. $K$ counts the number of parameters that are used in the model, including estimates of uncertainty in measured data.

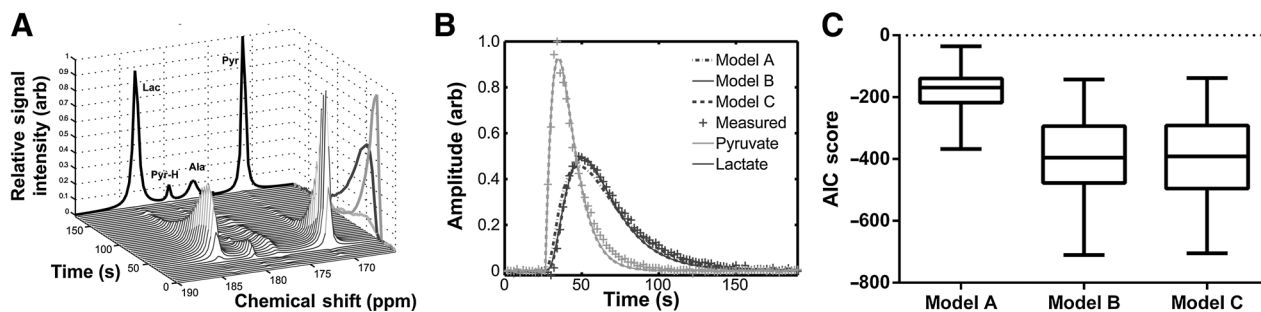### Constrained reconstruction of dynamic spectroscopic images

The constrained reconstruction algorithm allows direct substitution of kinetic models, with control variables to select parameters that may be assigned as known values rather than being allowed to vary. Radially-encoded $^1$H images were thresholded to distinguish between tissue and background regions that contribute no signal. In slices corresponding to tumor, 2D piecewise linear spatial basis functions, $\phi(\mathbf{r})$, were assigned to a synthetic image space with vertices separated by 2.2 mm on a square grid. Signal in the $N$ vertices associated with tissue were allowed to vary in time (30) according to the model, $\psi(\mathbf{p},t)$:

$$
\rho(\mathbf{r},\mathbf{p},\mathbf{t}) = \sum_{n=1}^N \phi_n(\mathbf{r})\psi(\mathbf{p}_n,\mathbf{t}) \quad (12)
$$

For direct measurement of the pyruvate vascular input function, radially-encoded $^1$H images traversing the heart were thresholded and manually segmented to identify regions corresponding to the heart, left ventricle (LV), and other tissues. The VIF was estimated by enforcing consistency between $^{13}$C measurements and signal estimated from these regions (23). The signal from these regions was assumed to decay exponentially since data acquisition was initiated after the injection was complete, and the exponential decay function corresponding to pyruvate signal in the LV was then used as a global VIF.

With the VIF explicitly measured, $T_1$ values for pyruvate and lactate assumed to be 45 and 25 seconds, respectively, and reverse chemical flux assumed negligible ($k_{lp} = 0$), the kinetic model illustrated in Fig. 2B requires six unknowns per basis function in order to describe dynamic evolution of HP pyruvate and lactate over time: $Pyr_{ev}(t=0)$, $Lac_{ev}(t=0)$, $k_{ve}$, $v_b$, $k_{pl}$, plus a scaling factor to account for sensitivity profile of the receive coil. Elimination of nonzero initial conditions, extravasation, and the intravascular volume fraction as unknowns reduced the number of unknowns to two per voxel. The constrained reconstruction algorithm solved for the $N\times6$ or $N\times2$ total set of parameter values that gave the lowest mean-square difference between measured data and signals that were predicted by this model when synthetic image space was sampled at corresponding points in time and with the same radial encoding strategy:

$$
\hat{\mathbf{p}} = \underset{\mathbf{p}\in\Re}{\arg\min}||\mathbf{s}(\mathbf{k},\mathbf{t}) - \mathbf{FR}\rho(\mathbf{r},\mathbf{p},\mathbf{t})||^2 \quad (13)
$$

Bankson et al.



**Figure 3.**
Comparison of model fits to observed data. The area under the spectral peaks (A) associated with pyruvate and lactate was integrated to generate dynamic summary curves. B, representative fits show subtle differences between models. C, in 55 datasets, models B and C (Fig. 2B and C) score significantly better (lower) than model A (Fig. 2A). Model B scored better than model C but not to statistical significance.

Synthetic raw data were generated by Radon ($R$) and Fourier ($F$) transform of the modeled dynamic image space.

## Results

Kinetic models were fitted to dynamic spectroscopic data from murine models of anaplastic thyroid cancer ($N = 27$) or normal matched anatomy ($N = 3$), triple-negative breast cancer ($N = 12$), and glioblastoma ($N = 10$) or normal brain ($N = 3$). Tumor metabolism was challenged using 2DG ($N = 9$; ref. 31), external radiation therapy ($N = 7$; ref. 32), or conditional gene expression ($N = 3$; ref. 19); controls were tested before or without perturbation ($N = 33$) or administered a negative control ($N = 3$). All three kinetic models fit these datasets ($N = 55$) reasonably well, as summarized in Fig. 3. AIC scores were higher (worse) for model A than for models B or C (corresponding to Fig. 2A–C, respectively) in aggregate ($P << 0.001$, paired $t$ test) and in each individual dataset. Although scores for models B and C were not statistically different in aggregate, scores for model B were slightly lower (better) on average and individually in 43 of 55 datasets. The additional computational burden inherent to model C is therefore not justified. Among these three candidates, the model composed of two physical and two chemical pools (Fig. 2B) has best overall agreement with our data from animal models of breast, brain, and thyroid cancer. The apparent exchange constant was higher when derived using model B compared with model A, across all datasets ($0.057 \pm 0.06$ vs. $0.048 \pm 0.041$; $P = 0.022$, paired $t$ test with $N = 55$) and within the largest cohort of similar data, from untreated ATC tumors ($0.039 \pm 0.025$ vs. $0.036 \pm 0.024$; $P < 0.001$, paired $t$ test with $N = 16$).

With a model in place, the intensity of HP signals in regions of space can be independently expressed as parameterized functions that are continuous in time (30). Multispectral constrained reconstruction that includes prior information from $^1$H MRI and enforces consistency between the dynamic image space and samples that are distributed in spatial frequency and temporal domains (Fig. 4) can restore spatiotemporal resolution from severely undersampled data. Figure 5 shows representative data acquired from a cohort of animals with anaplastic thyroid cancer. The vascular input function for HP pyruvate was derived by anatomically constrained estimation (23) from one slice that was prescribed to traverse the left ventricle. Figure 5C and D show the distribution of HP pyruvate and lactate in a slice containing

tumor; the combination (see Materials and Methods) of relatively high excitation angle, rapid temporal sampling, and high chemical conversion rate caused HP pyruvate within the tumor to have been attenuated to within the noise threshold by 2 seconds after the maximum of the HP lactate signal from tumor. This reconstruction approach solves directly for model parameters, which can easily be visualized as maps that overlay on anatomic images (Fig. 6) to concisely summarize the complex multidimensional data.

Certain model parameters may be derived from $^1$H data and eliminated as unknowns in the HP $^{13}$C reconstruction. Exploiting the similarity between Eq. (7) and the extended Tofts model for DCE-MRI, estimates for the fractional vascular blood volume ($v_b$) and pyruvate extravasation ($k_{ve}$) were calculated using a weighted average of high-resolution DCE-MRI parameter maps for fractional vascular blood volume ($v_b$) and Gd-DTPA extravasation ($K^{trans}$) over the set of spatial basis functions supporting the constrained reconstruction. Figure 7 shows representative results from the use of coregistered DCE-MRI parameters to inform on HP $^{13}$C signal evolution. Comparison of Figs. 6 and 7 show reduction in the number of unknowns that must be determined from HP $^{13}$C data by using an imaging sequence that allows data acquisition to begin before injection of the HP substrate and by use of model parameters that are derived in part from $^1$H MRI. Once parameters have been determined, the dynamic multispectral and multidimensional image space can be visualized with arbitrary temporal resolution (see Supplementary Video).

## Discussion

Dynamic nuclear polarization of [1-$^{13}$C]-pyruvate has tremendous potential as a new method for assessing cancer metabolism *in vivo*. Clinical translation of this powerful modality is underway (33). Data acquisition and reconstruction strategies must be thoroughly optimized and validated to ensure that observations can one day inform on clinical care. In this work, we explore models for HP signal evolution *in vivo* that approximate complex pharmacokinetics and support a framework for reconstruction of undersampled data, optimization of imaging strategies, and mitigation of key confounds. Our focus is on chemical exchange between HP pyruvate and lactate because this characteristic of aerobic glycolysis is often upregulated in cancer. Exchange between pyruvate and other
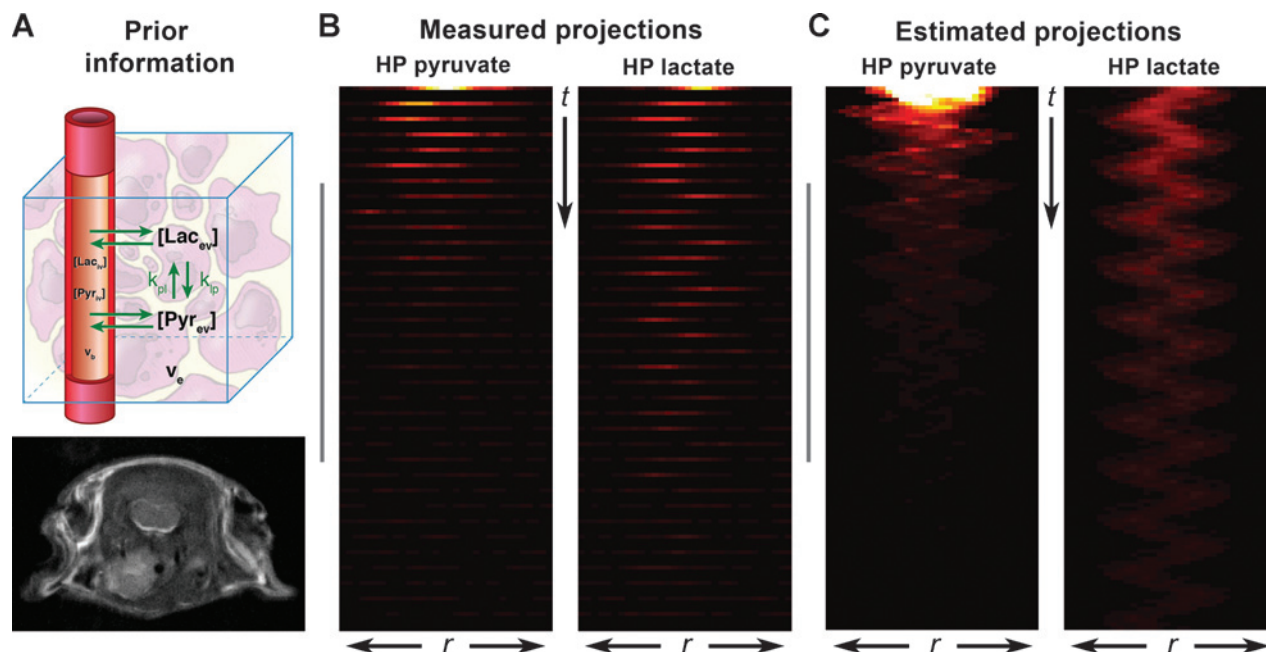
**Figure 4.**
Graphical summary of the model-based constrained reconstruction algorithm. A, temporal information from the kinetic model is combined with priors from
[1]H MRI to eliminate unknowns. The constrained reconstruction solves for model parameters that minimize the mean-square difference between estimates and under-sampled observations (B). C, estimates of signal at arbitrary time and position can then be calculated.

chemical endpoints can easily be incorporated. In lieu of their explicit inclusion, exchange of pyruvate to other pools is simply considered signal lost, accommodated by loss terms that are already present.

We propose a multispectral addition to the extended Tofts model to account for tumor perfusion and to sequester terms for metabolic activity, via exchange of the ^{13}C label between pyruvate and lactate, in the extravascular compartment. This is necessary to decouple the effects of perfusion on the HP lactate signal *in vivo* from metabolic activity that strictly depends on intracellular enzymes and metabolite pool sizes (11). Elimination of perfusion bias will improve the sensitivity and specificity of the metabolic quantitation that is driving diagnostic interest in this powerful new modality. In 55 measurements in normal and tumor-bearing mice, we show that this model with two physical compartments and two chemical pools (Fig. 2B) can be statistically selected, using Akaike's information criterion, as the most appropriate among the candidate models that were tested. Determination of reproducible rate constants for both extravasation and membrane transport from our test data using a higher-order model (Fig. 2C) would be more challenging, but it is certainly plausible that a PK model with three physical compartments and additional chemical pools could be a better choice under other experimental conditions.

Conversely, the selected model yielded a better AIC, lower residual differences to the HP lactate signal, and higher apparent conversion rates compared with the simpler precursor-product model (Fig. 2A). Kazan and colleagues (16) recently examined kinetic models for HP pyruvate that incorporate a vascular input function, but observed no statistically significant differences in $k_{pl}$ when comparing results from the simple precursor-product relationship (Case 6 in ref. 16) to those derived from the model fed by an explicitly measured input function (Case 1, Eqs. 6–9). Our model (Fig. 2B, Eqs. 6–8 above) differs in that signal in the vascular space, where the concentration of HP pyruvate is initially highest, remains an observable component of the overall signal in a compartment where chemical exchange is not permitted. Therefore a smaller fraction of the observed pyruvate signal is assumed able to interact with enzymes that catalyze exchange, and a higher apparent conversion rate is required to yield a given lactate signal. This approach eliminates the underestimation of apparent chemical conversion inherent to the simple precursor-product model, which assumes that all observed agents are in direct contact with target biology.

An informed kinetic model permits partial separation of spatial and temporal functions (30) that must be determined during the imaging measurement. The acquisition problem then changes from one of accurately sampling the spatial domain at a limited number of arbitrary times to one in which spatial and temporal domains must both be sampled appropriately. Parameterized models use fewer unknowns, and thus reduce the number of samples that must be obtained compared with naïve reconstruction of each point in time and space. Such a framework is vitally important in the observation of HP substrates because magnetization is changing continuously, not renewable, and depleted by the act of sampling itself. Prior information from ^{1}H MRI can also be integrated into the reconstruction algorithm to reduce the burden of new information that must be obtained from ^{13}C measurements.

Care must be taken in comparison of model parameters derived under differing conditions of prior information. Apparent conversion rates measured from animals bearing anaplastic

Bankson et al.
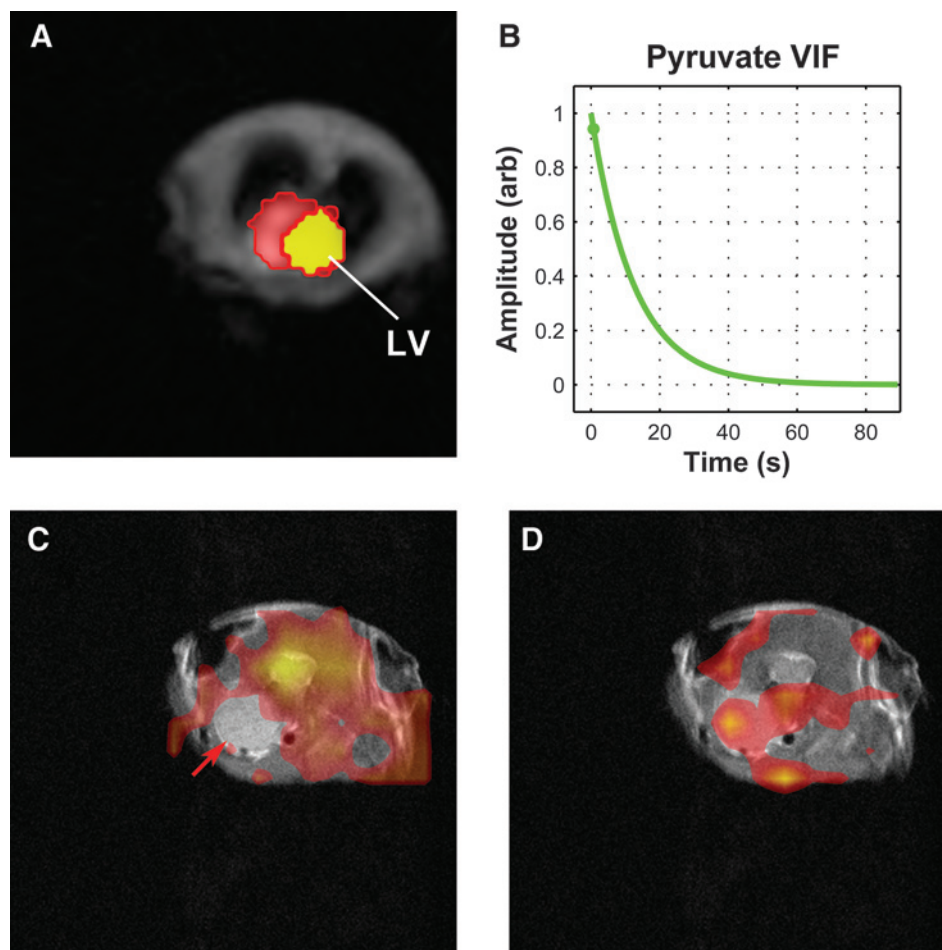
**Figure 5.**
Prior information and representative images from the model-based constrained reconstruction algorithm. A and B, segmentation of $^1$H MRI allows identification of the left ventricle (A) for constrained estimation of the pyruvate vascular input function (B). Once parameters are found, the kinetic model assists reconstruction of the distribution of HP substrates at arbitrary points in their observable life. Here, estimates for pyruvate (C) and lactate (D) are shown for $t = 6.4$s after the start of data acquisition, which followed injection and flush of HP pyruvate. Red arrow, tumor.

thyroid tumors using (a) dynamic spectroscopy with no assumption of prior information; (b) the double-spin echo MBFE sequence with concurrent measurement of the pyruvate VIF; and (c) the gradient-echo MBFE sequence with priors from DCE-MRI, as summarized in the Supplementary Table, show that rate constants can be significantly scaled by the
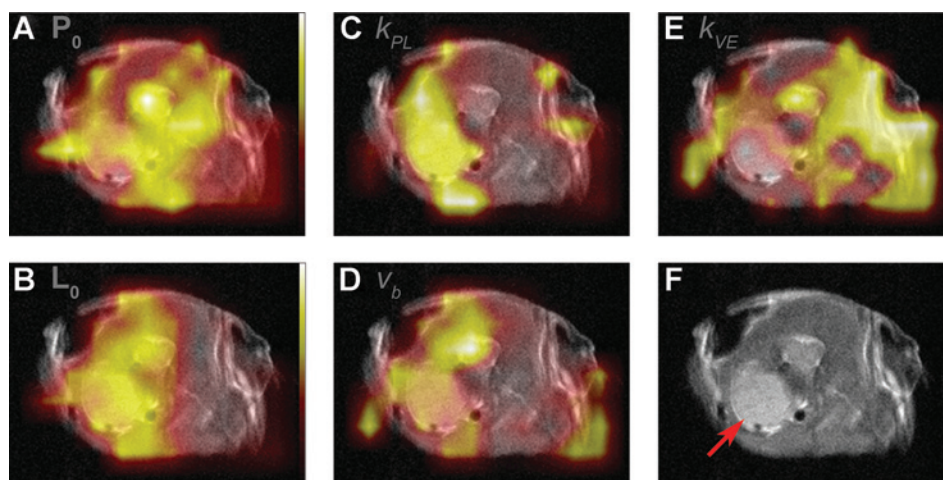


**Figure 6.**
Overlay of representative parametric maps derived from constrained reconstruction of radially encoded data from the double spin–echo MBFE sequence with interleaved measurement of the pyruvate vascular input function. A and B, $P_0$ (A) and $L_0$ (B) reflect the initial distribution of HP pyruvate and lactate at the start of data acquisition. C, $k_{pl}$, the rate constant (1/s) describing chemical conversion of pyruvate to lactate. D, $v_b$, the unitless fraction of tissue volume ascribed to the intravascular compartment. E, $k_{ve}$, the rate constant (1/s) for pyruvate extravasation. F, the background reference $T_2$-weighted image with ATC tumor is indicated by red arrow. All images were scaled to the maximum value of the associated parameter for ease of visualization, except for A and B, which were both normalized to the same value. Color bars along the right edge of these panels show the relative intensity scale.
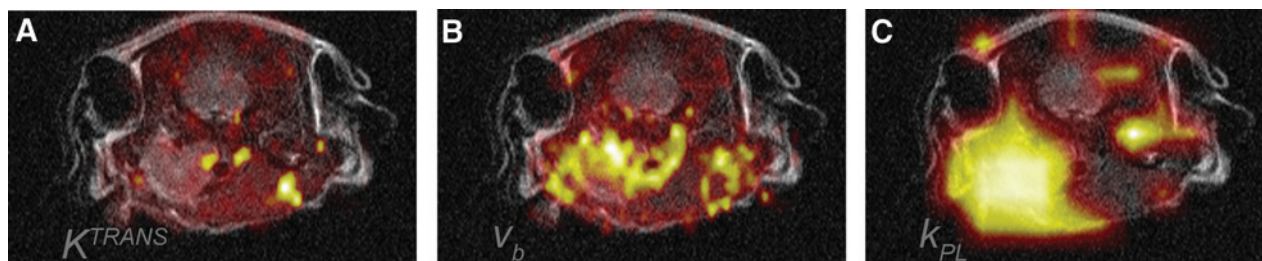
**Figure 7.**
Overlay of representative parametric maps derived from constrained reconstruction of gradient-echo radMBFE data with prior information from DCE-MRI. High-resolution parametric maps of $K^{trans}$ (A) and $v_b$ (B) from $^1$H DCE-MRI were used to eliminate unknowns for perfusion/extravasation and vascular volume fraction in the kinetic model for HP substrate evolution. C, $k_{pl}$, the apparent rate constant for chemical conversion of pyruvate to lactate.

information contained in priors that become integrated into the analysis and reconstruction. This scaling is not surprising, given the product relationship between the VIF, extravasation, and apparent conversion in formation of the HP lactate signal (Equation 7). We anticipate that consistent sets of prior information within a given cohort of measurements will permit comparison, and are exploring the impact of prior information, itself containing noise and potential bias, on the accuracy and reproducibility of measurements. We hypothesize that the significantly amplified conversion rate observed when $K^{trans}$ was used to estimate $k_{ve}$ (see Supplementary Table) is explained by a lower actual rate of extravasation for Gd-DTPA compared to pyruvate.

Assessment of spatial resolution is challenging for signals that are highly transient within the window of data acquisition. Resolution of images reconstructed by projection reconstruction of radially encoded data depends on the resolution along readout and the number of projections that are acquired. Projections for the data summarized in Fig. 7 had a nominal resolution along readout of 2.2 mm. Comparison of the appearance of a fiducial marker that was visible in both high-resolution Cartesian-encoded $^1$H and radially encoded $^{13}$C images revealed a Gaussian point spread function with a half-height full-width of approximately 3.7 mm due to the relatively short $T_2^*$ at 7T and the long readout window of the MBFE sequence. Estimation of image resolution from fiducial markers at thermal equilibrium that are visible in all projections likely represents an upper limit to spatial resolution for HP agents that are observable over a more limited range of projections.

The framework for model-based constrained reconstruction of HP substrates can be adapted to incorporate alternative kinetic models, pulse sequences, and encoding strategies. New sampling strategies or combinations of prior information will necessitate comparison of candidate models again to test whether the model summarized in Fig. 2b will remain the best choice. In this work, a radial encoding scheme was used with gradient-echo and double spin–echo imaging sequences. The double spin–echo MBFE sequence required delay of data acquisition until after administration of HP pyruvate, increasing the number of unknown model parameters to include terms for initial conditions. This delay also caused these measurements to miss the rising edge of HP signals, which is rich in information about extravasation and chemical conversion. Finally, we found that measurement of the pyruvate VIF in a broad slice through the heart and lungs significantly attenuated the HP signal in tumor; measurements using thinner slices and lower excitation angles would reduce that effect.

In summary, we propose a new pharmacokinetic model for dynamic evolution of HP substrates, and show for the first time that model-based constrained reconstruction enables visualization of HP pyruvate and lactate from dramatically undersampled raw data. This framework will be vital for the rational design of spatiotemporal sampling strategies as clinical translation of this technology expands. Variations to the model and to signal encoding and sampling strategies can easily be integrated into this reconstruction algorithm. The practical limitations of this approach are under investigation in simulation and using dynamic phantoms that mimic metabolic activity in normal and diseased tissues (12). Robust kinetic modeling and constrained reconstruction will significantly improve the accuracy and reproducibility, and thus the clinical potential, of metabolic imaging measurements using HP substrates such as pyruvate.

## Disclosure of Potential Conflicts of Interest

A. Rao is a consultant/advisory board member for GTCBio. No potential conflicts of interest were disclosed by the other authors.

## Authors' Contributions

**Conception and design:** J.A. Bankson, S.-C. J. Yeung, D. Schellingerhout, C.A. Conrad, C. Malloy, S.Y. Lai, J.D. Hazle
**Development of methodology:** J.A. Bankson, M.S. Ramirez, J. Lee, M.-H. Lee, D. Schellingerhout, C.A. Conrad, A.D. Sherry
**Acquisition of data (provided animals, acquired and managed patients, provided facilities, etc.):** J.A. Bankson, C.M. Walker, M.S. Ramirez, J. Lee, V.C. Sandulache, Y. Chen, L. Phan, P.-C. Chou, S.-C. J. Yeung, S.Y. Lai
**Analysis and interpretation of data (e.g., statistical analysis, biostatistics, computational analysis):** J.A. Bankson, C.M. Walker, M.S. Ramirez, W. Stefan, D. Fuentes, J. Lee, A. Rao, S.-C. J. Yeung, D. Schellingerhout, C.A. Conrad, C. Malloy, S.Y. Lai
**Writing, review, and/or revision of the manuscript:** J.A. Bankson, C.M. Walker, M.S. Ramirez, W. Stefan, D. Fuentes, M.E. Merritt, V.C. Sandulache, L. Phan, P.-C. Chou, D. Schellingerhout, C.A. Conrad, C. Malloy, A.D. Sherry, S.Y. Lai, J.D. Hazle
**Administrative, technical, or material support (i.e., reporting or organizing data, constructing databases):** J.A. Bankson, L. Phan, M.-H. Lee, J.D. Hazle
**Study supervision:** J.A. Bankson, M.-H. Lee, D. Schellingerhout, C.A. Conrad, S.Y. Lai, J.D. Hazle

Bankson et al.

## References

1. Ardenkjaer-Larsen JH, Fridlund B, Gram A, Hansson G, Hansson L, Lerche MH, et al. Increase in signal-to-noise ratio of > 10,000 times in liquid-state NMR. Proc Natl Acad Sci U S A 2003;100:10158–63.
2. Warburg O. On the origin of cancer cells. Science 1956;123:309–14.
3. Vander Heiden MG, Cantley LC, Thompson CB. Understanding the Warburg effect: the metabolic requirements of cell proliferation. Science 2009;324:1029–33.
4. Venkatanarayan A, Raulji P, Norton W, Chakravarti D, Coarfa C, Su X, et al. IAPP-driven metabolic reprogramming induces regression of p53-deficient tumours *in vivo*. Nature 2015;517:626–30.
5. Albers MJ, Bok R, Chen AP, Cunningham CH, Zierhut ML, Zhang VY, et al. Hyperpolarized 13C lactate, pyruvate, and alanine: noninvasive biomarkers for prostate cancer detection and grading. Cancer Res 2008;68:8607–15.
6. Day SE, Kettunen MI, Gallagher FA, Hu DE, Lerche M, Wolber J, et al. Detecting tumor response to treatment using hyperpolarized 13C magnetic resonance imaging and spectroscopy. Nat Med 2007;13: 1382–7.
7. Harris T, Eliyahu G, Frydman L, Degani H. Kinetics of hyperpolarized 13C1-pyruvate transport and metabolism in living human breast cancer cells. Proc Natl Acad Sci U S A 2009;106:18131–6.
8. Ward CS, Venkatesh HS, Chaumeil MM, Brandes AH, Vancriekinge M, Dafni H, et al. Noninvasive detection of target modulation following phosphatidylinositol 3-kinase inhibition using hyperpolarized 13C magnetic resonance spectroscopy. Cancer Res 2010;70:1296–305.
9. Khegai O, Schulte RF, Janich MA, Menzel MI, Farrell E, Otto AM, et al. Apparent rate constant mapping using hyperpolarized [1-13C]pyruvate. NMR Biomed 2014;27:1256–65.
10. Mariotti E, Veronese M, Dunn JT, Southworth R, Eykyn TR. Kinetic analysis of hyperpolarized data with minimum a priori knowledge: Hybrid maximum entropy and nonlinear least squares method (MEM/NLS). Magn Reson Med 2015;73:2332–42.
11. Witney TH, Kettunen MI, Brindle KM. Kinetic modeling of hyperpolarized 13C label exchange between pyruvate and lactate in tumor cells. J Biol Chem 2011;286:24572–80.
12. Walker CM, Lee J, Ramirez MS, Schellingerhout D, Millward S, Bankson JA. A catalyzing phantom for reproducible dynamic conversion of hyperpolarized [1-$^{13}$C]-pyruvate. PLoS ONE 2013;8:e71274.
13. Zierhut ML, Yen YF, Chen AP, Bok R, Albers MJ, Zhang V, et al. Kinetic modeling of hyperpolarized 13C1-pyruvate metabolism in normal rats and TRAMP mice. J Magn Reson 2010;202:85–92.
14. Hill DK, Orton MR, Mariotti E, Boult JK, Panek R, Jafar M, et al. Model free approach to kinetic analysis of real-time hyperpolarized 13C magnetic resonance spectroscopy data. PLoS ONE 2013;8:e71996.
15. Bahrami N, Swisher CL, Von Morze C, Vigneron DB, Larson PE. Kinetic and perfusion modeling of hyperpolarized (13)C pyruvate and urea in cancer with arbitrary RF flip angles. Quant Imaging Med Surg 2014; 4:24–32.
16. Kazan SM, Reynolds S, Kennerley A, Wholey E, Bluff JE, Berwick J, et al. Kinetic modeling of hyperpolarized (13)C pyruvate metabolism in tumors using a measured arterial input function. Magn Reson Med 2013;70:943–53.
17. Harrison C, Yang C, Jindal A, DeBerardinis RJ, Hooshyar MA, Merritt M, et al. Comparison of kinetic models for analysis of pyruvate-to-lactate exchange by hyperpolarized 13 C NMR. NMR Biomed 2012;25: 1286–94.
18. Gule MK, Chen Y, Sano D, Frederick MJ, Zhou G, Zhao M, et al. Targeted therapy of VEGFR2 and EGFR significantly inhibits growth of anaplastic thyroid cancer in an orthotopic murine model. Clin Cancer Res 2011;17: 2281–91.
19. Phan L, Chou PC, Velazquez-Torres G, Samudio I, Parreno K, Huang Y, et al. The cell cycle regulator 14–3-3sigma opposes and reverses cancer metabolic reprogramming. Nat Commun 2015;6:7530.
20. Ramirez MS, Lee J, Walker CM, Sandulache VC, Hennel F, Lai SY, et al. Radial spectroscopic MRI of hyperpolarized [1–13C] pyruvate at 7 tesla. Magn Reson Med 2014;72:986–95.
21. von Morze C, Reed G, Shin P, Larson PE, Hu S, Bok R, et al. Multi-band frequency encoding method for metabolic imaging with hyperpolarized [1-(13)C]pyruvate. J Magn Reson 2011;211:109–13.
22. Cunningham CH, Chen AP, Albers MJ, Kurhanewicz J, Hurd RE, Yen YF, et al. Double spin–echo sequence for rapid spectroscopic imaging of hyperpolarized 13C. J Magn Reson 2007;187:357–62.
23. Ragan DK, Lai SY, Bankson JA. Fast, reproducible measurement of the vascular input function in mice using constrained reconstruction and cardiac sampling. NMR Biomed 2011;24:373–84.
24. Kettunen MI, Kennedy BW, Hu DE, Brindle KM. Spin echo measurements of the extravasation and tumor cell uptake of hyperpolarized [1-13C]lactate and [1-13C]pyruvate. Magn Reson Med 2013;70:1200–9.
25. Larson PE, Hurd RE, Kerr AB, Pauly JM, Bok RA, Kurhanewicz J, et al. Perfusion and diffusion sensitive 13C stimulated-echo MRSI for metabolic imaging of cancer. Magn Reson Imaging 2013;31:635–42.
26. Tofts PS. Modeling tracer kinetics in dynamic Gd-DTPA MR imaging. J Magn Reson Imaging 1997;7:91–101.
27. Tofts PS, Brix G, Buckley DL, Evelhoch JL, Henderson E, Knopp MV, et al. Estimating kinetic parameters from dynamic contrast-enhanced T(1)-weighted MRI of a diffusible tracer: standardized quantities and symbols. J Magn Reson Imaging 1999;10:223–32.
28. Davenport R. The derivation of the gamma-variate relationship for tracer dilution curves. J Nucl Med 1983;24:945–8.
29. Akaike H. A new look at statistical-model identification. IEEE Trans Autom Control 1974;19:716–23.
30. Liang Z-P. Spatiotemporal Imaging with Partially Separable Functions. P IEEE Int Sym Bio-Med Imaging 2007 12–15 April 2007.
31. Sandulache VC, Skinner HD, Wang Y, Chen Y, Dodge CT, Ow TJ, et al. Glycolytic inhibition alters anaplastic thyroid carcinoma tumor metabolism and improves response to conventional chemotherapy and radiation. Mol Cancer Ther 2012;11:1373–80.
32. Sandulache VC, Chen Y, Lee J, Rubinstein A, Ramirez MS, Skinner HD, et al. Evaluation of hyperpolarized [1-$^{13}$C]-pyruvate by magnetic resonance to detect ionizing radiation effects in real time. PLoS ONE 2014;9:e87031.
33. Nelson SJ, Kurhanewicz J, Vigneron DB, Larson PE, Harzstark AL, Ferrone M, et al. Metabolic imaging of patients with prostate cancer using hyperpolarized [1–13C]pyruvate. Sci Transl Med 2013;5:198ra08.

# Cancer Research

**AACR** American Association for Cancer Research

# Kinetic Modeling and Constrained Reconstruction of Hyperpolarized [1- $^{13}$C]-Pyruvate Offers Improved Metabolic Imaging of Tumors

James A. Bankson, Christopher M. Walker, Marc S. Ramirez, et al.

| | |
|---|---|
| **Updated version** | Access the most recent version of this article at:<br>doi:10.1158/0008-5472.CAN-15-0171 |
| **Supplementary Material** | Access the most recent supplemental material at:<br>http://cancerres.aacrjournals.org/content/suppl/2015/09/29/0008-5472.CAN-15-0171.DC1.html |

| | |
|---|---|
| **E-mail alerts** | Sign up to receive free email-alerts related to this article or journal. |
| **Reprints and Subscriptions** | To order reprints of this article or to subscribe to the journal, contact the AACR Publications Department at pubs@aacr.org. |
| **Permissions** | To request permission to re-use all or part of this article, contact the AACR Publications Department at permissions@aacr.org. |